

Probing a cold surface with slow heavy-atom scattering: Experimental results and theoretical calculations

T. Andersson, F. Althoff, P. Linde, and S. Andersson

Department of Applied Physics, Chalmers University of Technology and Göteborg University, SE-412 96 Göteborg, Sweden

K. Burke

Department of Chemistry, Rutgers University, 610 Taylor Road, Piscataway, New Jersey 08854

(Received 3 May 2001; revised manuscript received 20 September 2001; published 2 January 2002)

Slow heavy atoms scattering from cold surfaces excite many phonons, but still have a finite elastic scattering fraction. We have measured the coherent elastic intensity of low-energy Ne, Ar, and Kr beams scattered from a Cu(111) surface, and compared the results to accurate semiclassical calculations. Earlier experiments have been extended to a range of incident beam energies, while earlier calculations have been improved by using state-of-the-art atom-surface potentials and surface phonon densities of states. All inputs to the calculations are taken from the literature, so they involve *no* adjustable parameters. We compare both the zero-temperature limit and the thermal attenuation of the elastic scattering at elevated temperatures. Our comparisons confirm that the probability for elastic scattering is (i) independent of particle mass m at low surface temperatures and (ii) depends on \sqrt{m} at elevated temperatures. Corresponding experimental observations for the comparatively light particles H_2 , D_2 , and He show clear deviations from the semiclassical predictions. Our analysis shows that this regime provides new and complementary information about both surface phonons and atom-surface potentials.

DOI: 10.1103/PhysRevB.65.045409

PACS number(s): 68.35.Ja, 34.50.Dy, 82.65.+r

I. INTRODUCTION

The scattering of light atoms, especially He, from solid surfaces has emerged as one of the major experimental tools for analysis of structural and vibrational properties of surfaces, by using the positions of elastic and inelastic scattering peaks in angular and energy-loss spectra.¹ However, the collision of a gas-phase particle with a solid surface also represents a canonical problem in many-body quantum mechanics. A finite fraction of particles undergoes coherent elastic scattering, an effect peculiar to quantum mechanics. This fraction is usually written e^{-2W} , where $2W$ is the Debye-Waller exponent. For x-ray scattering, which is fast and weak, this factor has a very simple form, but for atom-surface scattering, which is slow and strong, it is typically much more complex.²

In the common case of a light particle striking the surface with a given energy, the particle moves quickly and has significant momentum parallel to the surface. The scattering is weak and mostly elastic, and W is small. This case can be treated within a simple Born approximation (albeit using distorted waves, which include simple reflection from the surface), with no sophisticated many-body treatment.

But what happens to a heavy particle of fixed energy striking the surface? The immediate reaction is to think of classical behavior for large masses, so that no elastic fraction can survive. Indeed, this was found in the original calculations of Levi and Suhl,³ who showed that at finite surface temperature, $2W \propto \sqrt{m}T$, which diverges for large masses, yielding the classical result of zero elastic fraction. However, Burke and Kohn⁴ proved that, at zero temperature, $2W$ tends to a finite limit as $m \rightarrow \infty$. This prediction was recently confirmed⁵ by experiment, and was also found to hold in

more sophisticated quantum calculations^{6,7} than the original simple calculations of Burke and Kohn. Both the limiting value at zero temperature and the characteristic temperature scale on which the elastic peak rapidly decays have the predicted mass dependence.

In the present paper, a detailed comparison between theory and experiment illustrates that useful information about atom-surface potentials and surface phonons can be extracted from experiments in this regime. Instead of studying, e.g., bound-state resonances to find specific bound states of the physisorption well, we deduce values of classical momentum distributions, which depend sensitively on the shape and depth of the wells. Similarly, these experiments probe the long-wavelength regime of the surface-projected phonon density of states (DOS), rather than details of single modes at the surface.

The experiments for heavier particles (Ne, Ar, and Kr) are carried out at a low target temperature, around 10 K, using pulsed laser heating to prevent stuck particles from accumulating on the surface. We also discuss elastic scattering measurements for the comparatively light particles H_2 , D_2 , and He and compare our observations with those for the heavier inert gases. In this context, rotational excitations are unimportant for H_2 and D_2 ; these particles scatter like He at our impact conditions. On the other hand, heavier homonuclear molecules such as N_2 and O_2 reveal scattering patterns that are profoundly influenced by rotational excitations. These reduce both the elastic and the phonon inelastic scattering and couple strongly to diffraction and phonon excitations.⁸

We also extend the theory and calculations beyond the simple cases studied by Burke and Kohn. We show how to define and use effective physical parameters, which explain semiquantitatively all the trends seen in the accurate results. We use state-of-the-art parametrized potentials from accurate

electronic structure calculations. We find quantitative differences between these potentials and the commonly used Morse potentials. We also use an accurate density of states (DOS) for the Cu(111) surface. With these improvements, we can show the agreement with semiclassical predictions for heavier atoms and disagreement for lighter ones. We also show that the disagreement for lighter atoms stems largely from the excitation of phonons whose frequency is *not* small, so that for these cases, the surface response depends on the details of the surface DOS.

II. THEORY

When the mean energy transfer between an atom and the surface is small, the exponentiated distorted-wave Born approximation applies.⁹ Even if the scattering is strong, the Debye-Waller factor is then given by [cf. Eq. (19) of Ref. 4]:

$$2W(T) = \int_0^\infty d\omega \sum_{\mathbf{G}} \int \frac{d^2Q}{A_{\text{SBZ}}} |\langle \phi_{\mathbf{k}_i} | F_{\perp}(z) | \phi_{\mathbf{k}_f} \rangle|^2 \times \frac{\hbar}{2M_s \omega} \rho_{zz}(\mathbf{Q}, \omega) \coth\left(\frac{\hbar \omega}{2k_B T}\right), \quad (1)$$

where \mathbf{G} is a surface reciprocal lattice vector, \mathbf{Q} is the surface wave vector, A_{SBZ} is the surface Brillouin zone area, $F_{\perp}(z) = -dV_{\perp}(z)/dz$ is the derivative of the static potential, $\hbar/2M_s \omega$ is the amplitude of a surface vibration of frequency ω , where M_s is the mass of a surface atom, $\rho_{zz}(\mathbf{Q}, \omega)$ is the surface-projected density of states (DOS) of parallel momentum \mathbf{Q} and frequency ω , and $\coth(\hbar \omega/2k_B T)$ is a boson occupation factor, with k_B being Boltzmann's constant and T the surface temperature. Note that Eq. (1) assumes that only coupling to small wave vector phonons is significant (which is true for our case, as we show later). In that case, the curvature of the surface due to the phonon is slight, and so the incident particle experiences a force as if the static potential is rigidly shifted.

A. Large-mass limit

For heavy incident particles, the energy transfer between the particle and the surface becomes small, and we describe the scattering as quasiadiabatic. This does not mean that a small number of phonons are excited (in fact a finite number are), just that those phonons that are excited have small energies. This comes about because the incident particle exerts a slowly varying force on the surface, which can only excite phonons of low frequency. This allows several simplifications. First, the heavy incident particles behave classically, so that the quantum mechanical matrix elements of the distorted-wave Born approximation simplify to just the Fourier transform of the driving force on the surface generated by the incident particle (Appendix C of Ref. 4):

$$F_{\perp}(\omega) = \int_{-\infty}^{\infty} dt \exp(i\omega t) F_{\perp}(t). \quad (2)$$

Note that $F_{\perp}(\omega=0)$ is just the impulse delivered to the surface by the incident particle. Second, since only low-

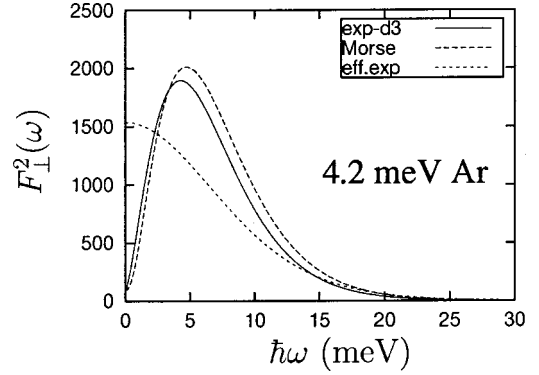


FIG. 1. Fourier transform of classical driving force for $E_{\perp} = 4.2$ meV Ar striking a cold Cu(111) surface, for several models of the atom-surface potential.

frequency phonons can be excited, only the low-frequency region of the surface-projected phonon density of states is sampled. We write the surface spectral function as

$$C_{zz}(\omega) = \frac{\hbar}{2M_s \omega} \rho_{zz}(\omega) \rightarrow C_s \omega \quad (\omega \rightarrow 0) \quad (3)$$

where

$$\rho_{zz}(\omega) = \sum_{\mathbf{G}} \int \frac{d^2Q}{A_{\text{SBZ}}} \rho_{zz}(\mathbf{Q}, \omega) \quad (4)$$

is the density of all phonons at the surface [$\int d\omega \rho_{zz}(\omega) = 1$]. The constant C_s is a simple characteristic elastic constant of the semi-infinite medium, independent of all atomistic details. Thus Eq. (1) becomes the semiclassical limit of Burke and Kohn:

$$2W(T) = C_s \int_0^\infty d\omega \omega F_{\perp}^2(\omega) \coth\left(\frac{\hbar \omega}{2k_B T}\right). \quad (5)$$

At zero temperature, the coth is just 1, and

$$2W(0) = C_s \int_0^\infty d\omega \omega F_{\perp}^2(\omega), \quad (6)$$

while at large temperatures, we find

$$2W(T) \rightarrow \beta T = \frac{2k_B T C_s}{\hbar} \int_0^\infty d\omega F_{\perp}^2(\omega). \quad (7)$$

Thus the zero-temperature and large-temperature limits of the Debye-Waller factor for a heavy atom contain extremely simple information about the atom-surface potential and the long-wavelength dynamics of the system. Furthermore, their ratio

$$2W(0)/\beta = \hbar \bar{\omega} / 2k_B \quad (8)$$

is independent of any details of the surface dynamics, and is a measure of the mean phonon energy contributing to $2W(0)$. (An alternative choice was made in Ref. 4.)

To illustrate better what is happening, in Fig. 1, we plot $F_{\perp}(\omega)$ from a calculation for 4.2 meV Ar atoms scattering

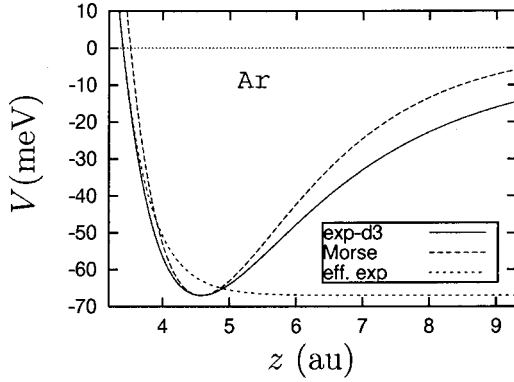


FIG. 2. Three different potentials for Ar hitting a Cu(111) surface: exp- $d3$ is our accurate potential, Morse has the same well depth and decay length, and eff. exp is a pure exponential repulsion, shifted downward by the well-depth, and with a reduced decay length ($d=0.55/\gamma=0.22$ Å, see Sec. III D) to mimic the exp- $d3$ case.

from the Cu(111) surface. The accurate potential (discussed later) shows a strong peak at around $\hbar\omega=5$ meV, after which it slowly decays. This frequency cutoff occurs because the collision is so slow that only these low-frequency phonons are excited by it. The frequency scale on which this happens can be estimated by noting that the effective incident energy E_{\perp} is about 70 meV, due to the 67 meV well depth, so each Ar atom has a velocity of about 600 m/s. In Fig. 2, we show several models for the potential, and see that the particle interacts with the surface over a length scale d of at least 1 bohr radius, so that the collision time is about 100 fs. Then \hbar/τ is about 6 meV. Crudely approximating $F_{\perp}(\omega)$ as a constant up to \hbar/τ , but vanishing at that frequency, and noting that $F_{\perp}(0)=2p_{\perp}$, the effective incident momentum, we obtain the qualitative estimates

$$2W(0) \approx 8E_{\perp}^2 C_s / d^2, \quad \beta \approx 2W(0) 4k_B \tau / \hbar. \quad (9)$$

Thus $2W(0)$ is independent of the incident mass, while β grows with the time scale of the collision, i.e., as \sqrt{m} .

B. Breakdown of large-mass limit

When do we expect this semiclassical limit to provide an accurate description of a real experiment? To begin with, we require conditions under which the driven oscillator model applies, i.e., small relative energy loss of the incident particle.⁹ In the semiclassical limit, the average energy loss is just [see just above Eq. (27) of Ref. 4, where it is denoted $\overline{\Delta E}$]

$$\Delta E = \hbar^2 C_s \int_0^{\infty} d\omega \omega^2 F_{\perp}^2(\omega). \quad (10)$$

If this loss is not too large a fraction of the incident particle's total energy, the driven oscillator model should be accurate. Under such conditions, a realistic fully quantal calculation can be performed for the atom-surface scattering.⁶ We can then ask, under which conditions will such a calculation be well-approximated by the simple semiclassical limit of

Burke and Kohn? First, the mass must be large enough, so that the wavelength is short compared to the length scale of the eigenstates of the potential, and a WKB approximation is valid (see Appendix C of Ref. 4). This leads to the driving force on the surface phonons being well approximated by that of the classical trajectory. Next, we require that the spectral function be linear in ω for all phonons excited significantly during the collision. Otherwise, the more general form of Eq. (3) must be used. Finally, we require that the parallel momentum transfer (and hence energy loss) be small, or else the dynamics cannot be treated as effectively one-dimensional. This effect is typically incorporated into a damping factor in the DOS (the Armand effect¹⁰), of the form $\exp(-Q^2/Q_c^2)$, where Q is the parallel momentum of the phonon, and Q_c is a cutoff factor depending on the incident atom. We explore all three sources of breakdown, showing they are small or negligible for the heavier atoms in our experiments.

III. CALCULATIONS

A. Details of calculations

All calculations reported in this paper were performed for a classical particle reflecting elastically from a one-dimensional surface. Inelastic, semiclassical, and three-dimensional effects were extracted from these trajectories, as detailed throughout this paper. First, the trajectory $z(t)$ is found by solving Newton's equation in the potential $V(z)$. We used the fourth-order Runge-Kutta procedure on a uniform grid in t . Subsequently, the time-dependent force is extracted on this grid and Fourier transformed to produce $F_{\perp}(\omega)$, which is then integrated to produce the various moments used in this paper. Because of the long-range attractive $1/z^3$ tail in the potential, we sometimes needed to go as far as 10 Å from the classical turning point, and used up to 10^7 points in a uniform grid to achieve good convergence of these moments. No calculation required more than a minute on a modern PC.

B. Realistic shape of the potential

For accurate, realistic calculations to compare with experiment, we use a form introduced by Chizmeshya and Zaremba (CZ) [Eqs. (3.22), (3.23), and (3.25) of Ref. 11]:

$$V_{\text{exp-}d3}(z) = A \exp(-\gamma z) - \frac{C_{\text{vdW}}}{(z - z_{\text{vdW}})^3} f_2(\gamma(z - z_{\text{vdW}})), \quad (11)$$

where C_{vdW} and z_{vdW} are the van der Wals constant and the reference plane origin, respectively. The damping factor $f_2(x) = 1 - \exp(-x)[1 + x(1 + x/2)]$ ensures that the attractive portion remains finite as $z \rightarrow z_{\text{vdW}}$. We denote this exp- $d3$, to indicate the exponential repulsion and a damped $1/z^3$ attraction. We adopt this form because it seems (from CZ's work) to be sufficiently complex to give a realistic model for the potential, while being characterized by three simple parameters: γ , an inverse length; D , the well-depth; and finally a dimensionless parameter

TABLE I. Potential parameters as specified in Secs. III B and III C.

	C_{vdW} (eV a_0^3)	z_{vdW} (a_0)	A (eV)	γ (a_0^{-1})	η	z_{min} (a_0)	D (meV)
H ₂	4.540	0.3200	7.614	1.260	1.785	4.424	29.50
D ₂	4.540	0.3200	7.614	1.260	1.785	4.424	29.50
He	1.529	0.3237	6.999	1.333	0.7966	5.571	6.100
Ne	3.059	0.3146	7.133	1.348	1.605	4.345	22.00
Ar	10.39	0.3754	24.78	1.313	1.554	4.573	67.01
Kr	14.64	0.3978	30.51	1.293	1.735	4.452	99.99

$$\eta = C_{\text{vdW}} \gamma^3 \exp(\gamma z_{\text{vdW}}) / A, \quad (12)$$

which characterizes the shape of the potential. Smaller values of η give broader potentials, larger values give narrower ones. This is an extra degree of freedom, missing from a simple Morse potential. The canonical form is then

$$V(z) = D \nu(x) / |\nu_{\text{min}}|, \quad (13)$$

where $x = \gamma(z - z_{\text{vdW}})$, and

$$\nu(x) = \exp(-x) - \eta f_2(x) / x^3, \quad (14)$$

with ν_{min} being its minimum value. We chose this form over the alternative suggested by CZ [their Eq. (3.24)], because that alternative requires a second dimensionless parameter, but does not appear any more accurate.

C. Best values for potential parameters

The potential parameters are listed in Table I, where the position of the potential minimum, z_{min} , refers to the jellium edge.¹² For each of the incident atoms He, Ne, Ar, and Kr, we use the values of γ and η from the potentials of CZ. For incident molecules H₂ and D₂, we chose values for γ and η from potentials deduced from selective adsorption measurements.¹³ But for all well depths, we use the most recent information deducible from experiment, which yields wells slightly deeper than those reported by CZ. For H₂, D₂, and He interacting with copper surfaces detailed information about the potentials is available from selective adsorption measurements. The well depth for H₂ and D₂ on Cu(111) is $D_{\text{H}_2} = 29.5$ meV.¹³ Selective adsorption measurements for He scattered from the stepped Cu(113) and Cu(115) surfaces give almost identical sequences of well states compatible with a He-Cu interaction potential with $D_{\text{He}} = 6.3$ meV.¹⁴ During the course of the experiments discussed in this paper we determined the He-Cu potential for the flat Cu(110) surface from selective adsorption measurements.¹⁵ Using beams of both ³He and ⁴He we obtained a unique level assignment compatible with a single gas-surface potential for the two isotopes and a well depth of $D_{\text{He}} = 6.1$ meV. The best experimental physisorption potential data we have found for Ar and Kr refer to equilibrium thermodynamic measurements in the limit of low surface coverage on Ag(111), which give $D_{\text{Ar}} = 74$ meV and $D_{\text{Kr}} = 110$ meV.¹⁶ We judge that these values are slightly too large with respect to a Cu(111) substrate. The

well depths for H₂ on Cu(111) and Ag(111) are 29.5 meV (Ref. 13) and 32.5 meV (Ref. 17), respectively, as determined from selective adsorption measurements. Adjusting the well depths for Ar and Kr accordingly we arrive at $D_{\text{Ar}} = 67$ meV and $D_{\text{Kr}} = 100$ meV on Cu(111). No experimental data are available for Ne adsorption on either Cu(111) or Ag(111). We have observed from thermal desorption measurements that Ne desorbs from Cu(111) at a temperature that is only slightly lower, 1–2 K, than the H₂ desorption temperature just above 10 K. This indicates that the well depths for Ne and H₂ on Cu(111) are rather similar. The ground state energy for H₂ on Cu(111) is -23.9 meV.¹³ We estimate from the lower desorption temperature a corresponding energy of -20 meV for Ne. Adding a zero point energy of 2 meV gives a well depth of 22 meV.

D. Effective potentials

While all our comparisons with experiment are done with the accurate $\exp(-d^3)$ potential, we find that the results can be semiquantitatively understood by a Beeby-type correction to an exponential repulsion,

$$V_{\text{exp}}(z) = A \exp(-z/d). \quad (15)$$

For the ranges of parameters used here, we have found that $2W(0)$ and β [Eqs. (6) and (7)] are well approximated by scattering from an exponential repulsion, but with effective normal energy $E_{\text{eff}} = E_{\perp} + D$, and $d = 0.55/\gamma$. The first correction has an obvious physical significance, being the total perpendicular energy as measured from the bottom of the attractive well. The second correction states that the effective length scale is only a little more than half the decay length of the repulsive exponential in the accurate potential. This is because the rise of the repulsive wall in the accurate potential, from the potential minimum to the classical turning point, is more rapid than that of a simple exponential, as can be seen in Fig. 2. The exponential repulsion yields an impulse function

$$F_{\perp}(\omega) = p_{\perp} \frac{2\pi\omega\tau}{\sinh(\pi\omega\tau)}. \quad (16)$$

Insertion into Eqs. (6) and (7) yields

$$2W(0) = \alpha I_1, \quad \beta = \frac{k_B 2\alpha\tau}{\hbar} I_0, \quad (17)$$

where $\alpha = 4E_{\perp}^2 C_s / d^2$, and $I_0 = 2\pi/3 = 2.094$, $I_1 = 6\zeta(3)/\pi^2 = 0.731$, $I_2 = 2\pi/15 = 0.4189$, etc., are constants characteristic of the shape of the potential, where ζ is the Riemann zeta function (note slight inaccuracies in the numbers reported in Table 1 of Ref. 4). Replacing E_{\perp} by E_{eff} and noting that $\tau \approx d/v_{\perp}$, where v_{\perp} is the particle's velocity normal to the surface, we have $2W(0) \propto E_{\text{eff}}^2$ and does not depend on m while $\beta \propto \sqrt{m} E_{\text{eff}}^{3/2}$.

We will also compare our results with those of a simple Morse potential

$$V_{\text{Morse}}(z) = D[\exp(-\gamma z) - 2\exp(-\gamma z/2)]. \quad (18)$$

This has two independent physical parameters, a decay length and a well depth, but there is no way to adjust the shape. This form of potential is popular, and was used both in the original comparison⁵ and by Siber and Gumhalter.⁶ However, it lacks the slowly decaying attractive tail of the true potential and has the wrong shape. As we show in our calculations below, this leads to quantitative errors, so that the Morse potential is no more accurate than the effective exponential mentioned above, and less useful, since the effective exponential yields simple results with a simple interpretation.

In Fig. 2, we plot all three potentials for 4.2 meV Ar incident on a Cu(111) surface. The Morse potential agrees well with the accurate $\exp(-d^3)$ potential for z between the minimum and the turning point, but decays far too rapidly for large z . At best, it can be used for semiquantitative arguments. But for that purpose, the effective exponential is more appropriate. Even though its potential looks quite different, the impulse function, shown in Fig. 1, is quite similar to the accurate curve. Thus the effective exponential model allows us to easily understand qualitative trends in the results (see Sec.V), providing explanations of trends, quick rough estimates of corrections, etc.

E. Phonon spectral function at surface

To calculate the large-mass results, the only information we need about the phonon spectral function at the surface is the constant C_s , which characterizes the low-frequency behavior of this response. Thus this constant is an elastic constant of the semi-infinite crystal, and has no dependence on any atomic details, such as the surface and steps. In principle, it is simply calculable from the elastic constants of the bulk medium. Here we use the accurate estimate of Burke and Kohn $C_s = 0.0754 \times 10^{-4} \text{ \AA}^2/\text{meV}^2$. This compares well (to within about 20%) with values from more recent calculations of this quantity.¹⁸ But such calculations are based on short-ranged forces between atoms, and so will be less reliable for small ω than elastic continuum calculations.

IV. EXPERIMENT

In this section we describe gas-surface scattering experiments that measure the low-temperature behavior of the Debye-Waller factor. This requires measurements performed at such low target temperatures that the probe particles, with few exceptions, will stick permanently and accumulate on the target surface. Adsorbed particles will then quickly blur the coherent scattering and the useful data collection time becomes too short. A simple remedy for this complication is to desorb the stuck particles by laser pulses of short duration so that the mean surface temperature is marginally affected. We have for this purpose used a Lambda Physik XeCl excimer laser operating at a laser power $< 3 \text{ MW/cm}^2$ and 20 ns pulse duration. Repetition rates around a few hertz is in general sufficient to keep the surface clean. The laser beam hits the surface close to normal incidence and the reflected beam exits via the entrance window. At the surface temperatures of concern the surface ordering is unaffected by the laser irra-

diation as revealed by specular elastic scattering measurements with and without laser heating at a specimen temperature kept slightly above (around 20 K for H_2 , D_2 and Ne, 40 K for Ar and N_2 , and 60 K for Kr) that required for thermal desorption. At lower temperatures we routinely use laser desorption to prevent stuck beam particles from accumulating on the surface. The low binding energy of He makes it possible to perform the scattering experiment at a target temperature of 10 K without resorting to the laser desorption method. We can thus use specular He scattering as a measure of any induced damage caused by the laser irradiation.¹⁹ Examples of such measurements will be presented and discussed below.

The scattering experiments were carried out in a cryopumped ultrahigh vacuum chamber operating at a base pressure of 2×10^{-11} Torr and attached to a differentially pumped nozzle beam source. Incident and scattered beam intensities were measured using a rotatable stagnation detector with an angular resolution of 0.8° . The angular divergence of the incident beam is about 0.1° . Beam energies were determined by performing diffraction measurements using the same detection system. The x-ray aligned ($< 0.2^\circ$) and polished Cu(111) specimen was cleaned in the ultrahigh vacuum chamber by standard methods involving argon-ion bombardment and heating cycles. Using helium as a cryogen the specimen could be cooled to temperatures below 10 K and it was heated resistively. The crystal surface was oriented so that, at off-normal incidence, the scattering plane defined by the incident and specular particle beams comprised the surface normal and the $[11\bar{2}]$ direction in the surface plane. Further details concerning the apparatus, the specimen preparation, and the experimental procedure are presented elsewhere.²⁰

Atomic-scale restructuring via production of adatoms and vacancies, of low-index copper surfaces by nanosecond laser pulses of green light has recently been reported by Ernst, Charra, and Douillard.¹⁹ Notably they observed, via specular He scattering, surface defect production at relatively low specimen temperatures (90–300 K) and for a moderate laser-induced surface temperature rise (115 K). We have performed similar measurements in order to characterize our laser desorption conditions. The specular He reflectivity from the clean, well-ordered, and cold Cu(111) surface is high, almost unity, and very sensitive to induced atomic scale defects for our scattering conditions.²¹ The He beam energy is 36 meV and the angle of incidence is 70° from the surface normal.

Figure 3 displays the specular He reflectivity, I_{00} , from Cu(111) versus time with and without laser irradiation at a few target temperatures of interest. The initial reflectivity is normalized to unity. We have used the same power and repetition rate of the XeCl excimer laser as in the laser desorption work, that is, 2.3 MW/cm^2 and 3 Hz, respectively. In the temperature range 10–40 K the He reflectivity remains unaffected for typical measurement times of order 100 s and we judge that laser-induced damage is negligible in this temperature range. At 80 K however, the He reflectivity drops by about 10% after 100 s of pulsed laser irradiation, the defect concentration is estimated to be of the order of 0.5% of the

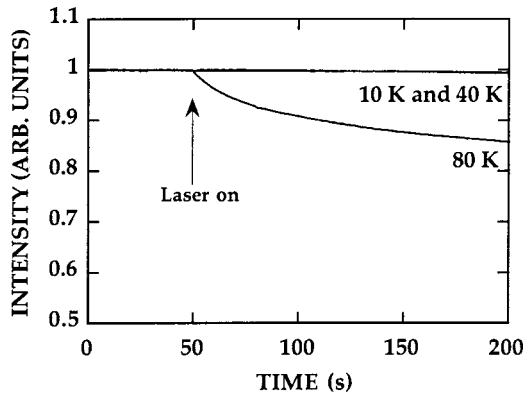


FIG. 3. Specular helium peak intensity versus time of XeCl excimer laser irradiation observed for a Cu(111) surface kept at 10, 40, and 80 K. The energy of the incident helium beam is 36 meV and the angle of incidence is 70° from the surface normal. The intensity is normalized at the initial values. The laser power is 2.3 MW/cm^2 and the repetition rate is 3 Hz.

surface atoms.²¹ The maximum surface temperature change due to the laser pulse is estimated to be around 60 K as found from the heat diffusion model.^{22,23} At the modest desorption temperatures required in our low-temperature scattering measurements laser-induced damage presents no disturbance.

V. RESULTS AND DISCUSSION

A. Experiments

At a low target temperature around 10 K the scattering pattern for heavy particles such as Ar and Kr exhibits sharp features due to elastic scattering events. This behavior is illustrated in Fig. 4, which displays in-plane angular distributions for Ne, Ar, and Kr beams scattered from the Cu(111) surface at different target temperatures. The scattered intensity in Figs. 4–6 is normalized to the intensity of the direct beam. The angle of incidence is 70° from the surface normal and the particle energy is 36 meV. Distributions measured at low temperature reveal sharp elastic features such as a specular peak and first-order diffraction peaks around 52° , 56° , and 60° for Ne, Ar, and Kr respectively. There is also a broad phonon emission peak around 76° – 78° . For Ar and Kr the sharp elastic peaks decrease quickly in intensity when the target temperature is increased; at 84 K and 42 K, respectively, only a weak specular peak superimposed on a broad inelastic background remains.²⁴ The elastic Ne scattering is much less affected at these temperatures but is significantly reduced at 300 K. At higher temperatures the specular peak for Ar and Kr becomes very weak compared to the inelastic background. The peak shape remains well defined though with an angular width around 1° , which is the same as the width of the direct beam peak and the specular beam peak otherwise. We have determined the peak intensity by subtracting off an extrapolated background as shown in Fig. 5. A second-order polynomial fit to the inelastic background outside the peak defines the background level.

We compare the elastic scattering of Ne, Ar, and Kr at different target temperatures with the behavior for lighter

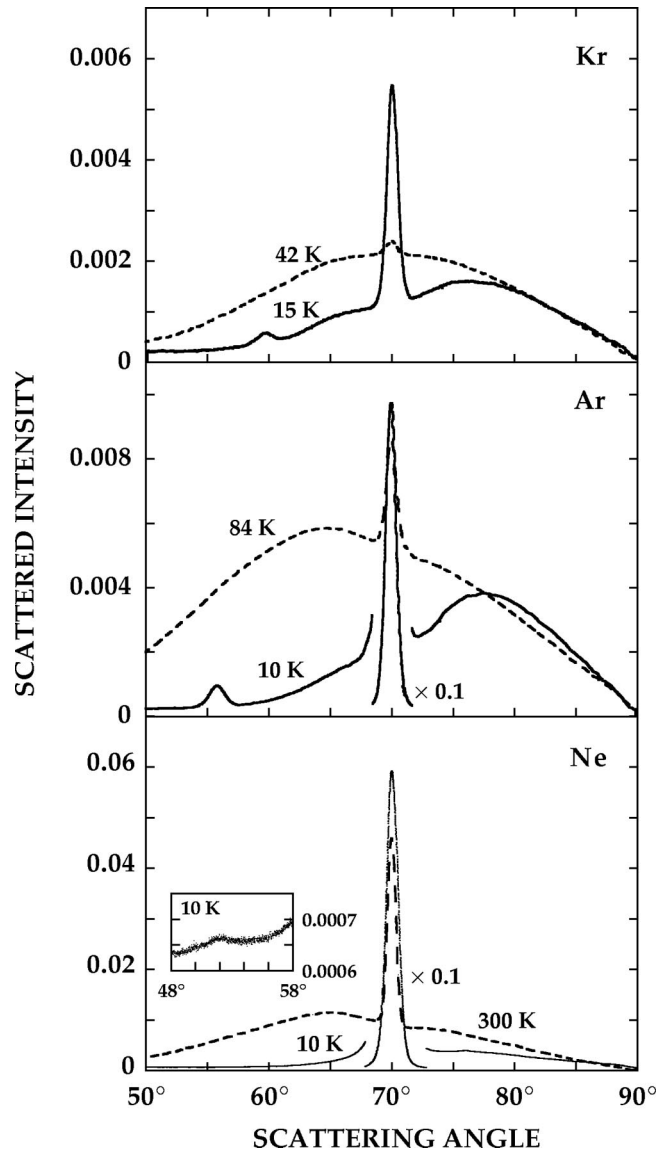


FIG. 4. Measured angular distributions for Ne, Ar, and Kr scattered from a Cu(111) surface at different temperatures. The energy of the incident particle beam is 36 meV and the angle of incidence is 70° from the surface normal. The scattered intensity is normalized to the intensity of the direct beam.

particles such as He, H_2 and D_2 . The hydrogen molecules are in fact suitable light test particles; the predominant scattering pattern resembles that of the inert gases; rotational and vibrational excitations are unimportant at our scattering conditions. This is not the case for heavier diatomic molecules such as N_2 and O_2 . Their scattering patterns are profoundly influenced by inelastic processes involving rotational excitations. Figure 6 displays in-plane angular scans measured for D_2 and N_2 beam scattering. The target temperature is 10 K and the impact conditions are the same as that for the inert gases discussed above. The D_2 data show a prominent specular elastic peak, a weak first-order diffraction peak around 37° , and a very weak $2 \rightarrow 0$ rotational inelastic peak around 48° . The low-temperature scan for N_2 exhibits a diffraction peak at 54° and a rich structure of rotationally inelastic scat-

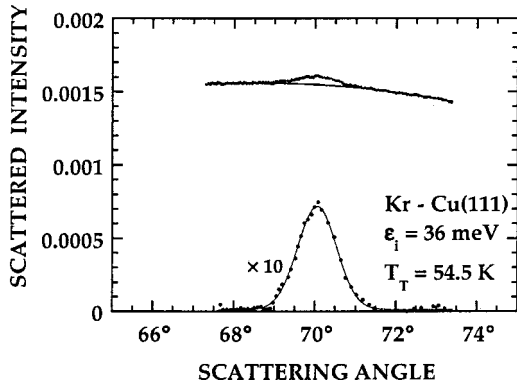


FIG. 5. Specular peak angular scan, as measured and after background subtraction, for Kr scattered from Cu(111) at 54.5 K. The scattered intensity is normalized to the intensity of the direct beam.

tering peaks. These inelastic scattering channels drastically reduce the elastic scattering probability.⁸ The sharp features in the N₂ data are quickly smeared out when the target temperature is increased, just as we observed for Ar and Kr. We notice in this context that rotationally inelastic diffraction is a well-established phenomenon in scattering of hydrogen molecules²⁵ and we discuss such scattering for N₂ and other molecules (D₂, O₂, and CH₄) in detail elsewhere.⁸

Diffraction peaks are weak relative to the specular peak in the angular scans shown in Figs. 4 and 6. This just reflects that Cu(111) is an electronically smooth surface. Hence we

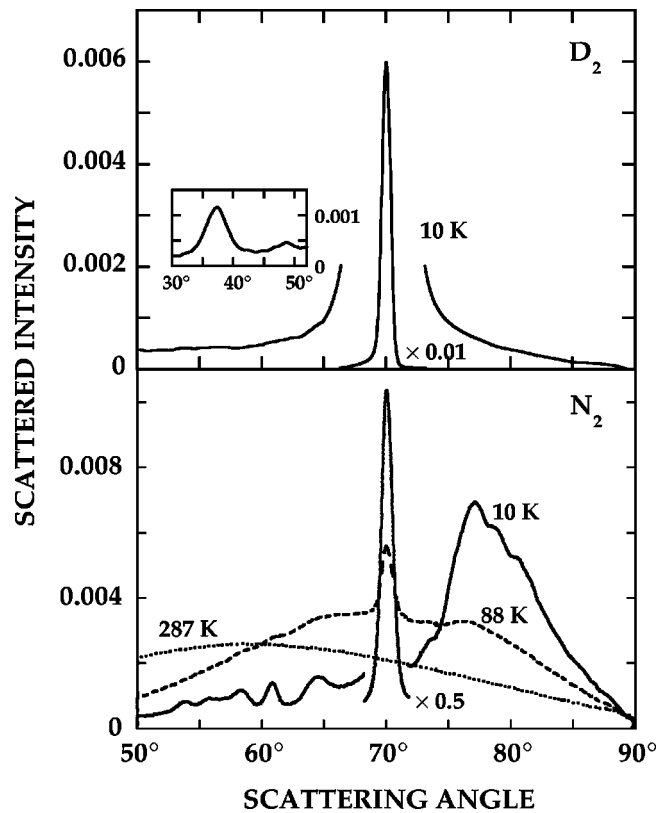


FIG. 6. Measured angular distributions for D₂ and N₂ scattered from a Cu(111) surface at different temperatures. Conditions as in Fig. 4.

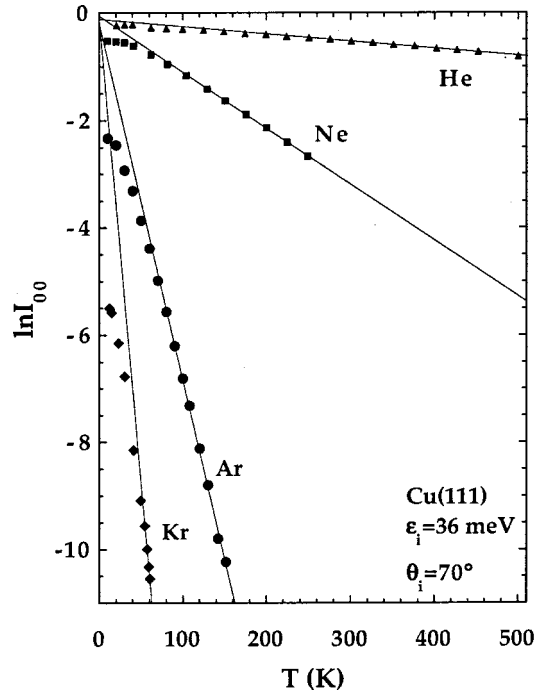


FIG. 7. Normalized specular reflectivity I_{00} , plotted as $\ln I_{00}$ versus target temperature T for He, Ne, Ar, and Kr. Incidence conditions as in Fig. 4. The straight lines, extrapolated to $T=0$, are fits to the linear decay of $\ln I_{00}$.

can regard the specular elastic peak as a good measure of the elastically scattered fraction, which is given by the Debye-Waller factor e^{-2W} . We will consider the temperature dependence of the elastic scattering in a more quantitative way starting from the data shown in Figs. 7 and 8. Here we have plotted the normalized specular reflectivity I_{00} for He, Ne, Ar, Kr (Fig. 7) and H₂, D₂, N₂ (Fig. 8) as $\ln I_{00}$ versus target temperature. Incidence conditions are the same as those for the angular scans in Figs. 4 and 6. The accuracy in a specific measurement yields typical errors that are smaller than the size of the data points. These plots (except for N₂) simply reflect the influence of e^{-2W} on I_{00} . Towards higher temperatures $\ln I_{00}$ decays in an approximately linear fashion, $2W = \beta T$ for all the particles.²⁶ Extrapolating the linear decay of $\ln I_{00}$, for He, Ne, and Ar in Fig. 7 to $T=0$ K we find that $\ln I_{00}$ is around -0.1 rather than 0 as we would expect for a rigid lattice in a case of weak diffraction. We believe that this deviation is due to diffuse elastic scattering caused by surface imperfections. The linear decay of $\ln I_{00}$ for H₂ and D₂ in Fig. 8 also extrapolates to $\ln I_{00}$ around -0.1 at $T=0$ K. The N₂ data behave in a strikingly different manner. Extrapolating the linear decay to $T=0$ K gives a value of $\ln I_{00}$ around -2.9 , a difference we attribute to rotationally inelastic scattering,⁸ which strongly reduces the elastic scattering of N₂. H₂ and D₂, on the other hand, behave just like the inert gases, which implies that rotational excitations are unimportant for these particles at our impact conditions.

At lower temperatures all the plots in Figs. 7 and 8 deviate from a linear behavior and eventually level off at approximately temperature-independent values. We may fit the low-temperature region of the $\ln I_{00}$ data with a Gaussian

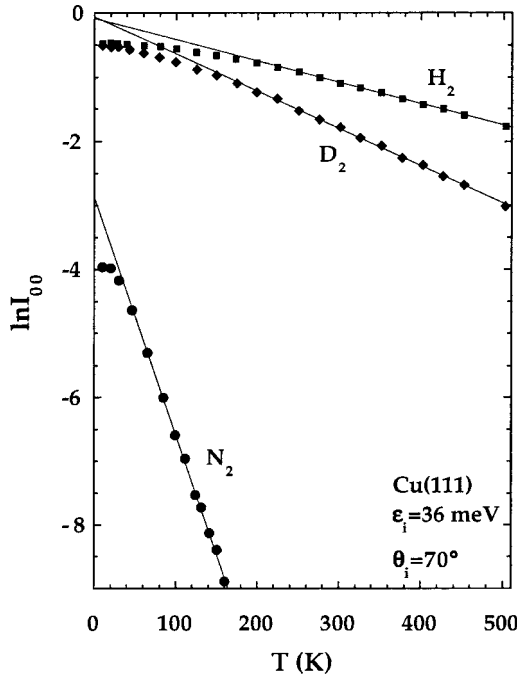


FIG. 8. Normalized specular reflectivity I_{00} , plotted as $\ln I_{00}$ versus target temperature T for H_2 , D_2 , and N_2 . Incidence conditions as in Fig. 4. The straight lines, extrapolated to $T=0$, are fits to the linear decay of $\ln I_{00}$.

function of T and extract $2W$ at $T=0$ K from this function. These values of $2W(0)$ are almost identical to the values at 10 K except for Kr in which case $2W=5.2$ at 0 K while the measured 10 K value is 5.5. This difference reflects a slight increase in $\ln I_{00}$ from 10 K to 0 K, which is also evident in the calculations presented in Ref. 4. The correction is rather small, however, and we adopt the measured values at 10 K as good low-temperature estimates of $2W(0)$. In Table II we have listed these experimental data together with the experimental linear decay parameter β obtained in the temperature ranges discussed in Ref. 26. The experimental $2W(0)$ data are reduced by 0.1 for the zero level correction discussed above. The accuracy of $2W(0)$ is 7–8% for H_2 , D_2 , and Ne and 4–5% for Ar and Kr. Corresponding values for β are around 5% for H_2 , D_2 , Ne, and Ar and around 7% for Kr. These numbers give the experimental error bars in Figs. 9–12. The He data are particularly sensitive to the influence of diffuse elastic scattering caused by surface imperfections. This is so because both $2W(0)$ and β attain small values for He, 0.1 and 0.0014, respectively. A typical uncertainty of the zero-level correction of order 0.02 will only be of importance for He. Likewise small temperature-dependent changes of the surface perfection will introduce a small uncertainty in the slope determination, which will only be of importance for He because of the small β value. D_2 , which also is a mass-4 particle, is clearly less sensitive to these effects and we have in the discussion below used the data for D_2 rather than for He.

B. Comparison with semiclassical limit

Table II also displays $2W(0)$ and β calculated for the accurate exp-d3 potentials discussed in Sec. III B. These are

TABLE II. Results for $2W(0)$ and β , both experimental and semiclassical limit continuum theory calculations with accurate potential (exp-d3), as a function of incident atom mass m , and energy E_{\perp} .

	m (amu)	$2W(0)$		β (K^{-1})	
		Calc.	Expt.	Calc.	Expt.
$E_{\perp} = 4.2$ meV					
H_2	2.0	0.52	0.34	0.0047	0.0033
D_2	4.0	0.52	0.39	0.0066	0.0058
He	4.0	0.04	0.10	0.0010	0.0014
Ne	20.2	0.35	0.35	0.0107	0.0109
Ar	40.0	2.57	2.23	0.0679	0.0670
Kr	83.8	5.51	5.40	0.1743	0.1670
E_{\perp} (meV)					
Ne	4.2	0.35	0.35	0.0107	0.0109
Ne	10.0	0.46	0.43	0.0136	0.0133
Ne	20.0	0.70	0.57	0.0190	0.0183
Ne	30.0	0.97	0.77	0.0249	0.0230
Ar	4.2	2.57	2.23	0.0679	0.0670
Ar	10.0	2.88	2.39	0.0743	0.0728
Ar	15.0	3.15	2.50	0.0800	0.0788
Ar	20.0	3.43	2.67	0.0859	0.0841

listed for all our different incident atoms, in order of increasing mass, and for both Ne and Ar, as a function of incident energy. The trends in these comparisons are best seen in a sequence of figures. We first consider β , the decay rate at high temperature, because it is the more accurately predicted of the two values. We note that β varies over a wide range in the experiments. This variation can be easily understood in terms of the effective exponential model, Eq. (17), with $E_{\text{eff}} = E_{\perp} + D$ and $d = 0.55/\gamma$. In this rough model, $\beta \propto \sqrt{m} E_{\text{eff}}^{3/2}$, where the proportionality constant depends only on the surface response. Thus, to see the mass dependence, without the dependence on the effective incident energy brought about by the large range of well depths, we scale β by $(E_{\text{eff}}^{\text{Ar}}/E_{\text{eff}})^{3/2}$, where the $E_{\text{eff}}^{\text{Ar}} = 4.2 + 67 = 71.2$ meV, and plot the scaled β versus \sqrt{m} . The linear dependence ob-

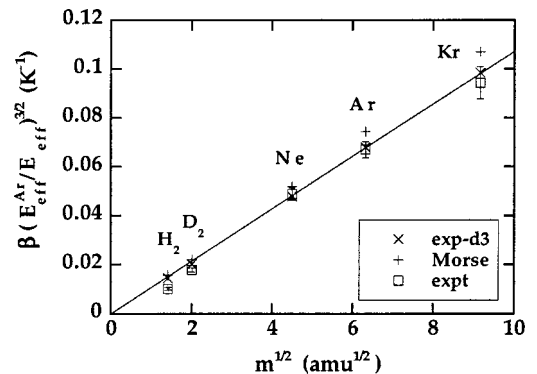


FIG. 9. High-temperature decay rate, β , of the Debye-Waller factor as a function of \sqrt{m} , scaled by $E_{\text{eff}}^{3/2}$. The points at $m=4$ refer to D_2 . The straight line is a guide for the eye.

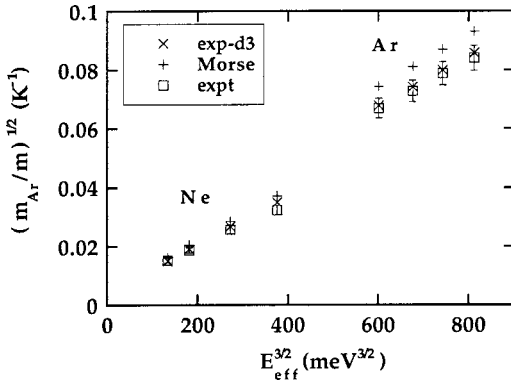


FIG. 10. High-temperature decay rate, β , of Debye-Waller factor scaled by \sqrt{m} as a function of $E_{\text{eff}}^{3/2}$, for incident Ne and Ar atoms.

served in Fig. 9 clearly demonstrates the \sqrt{m} behavior and also shows that, for masses larger than 4, the calculations agree very well with experiment. Note that the data points at $m=4$ refer to D_2 , not He. Also plotted are results with Morse potentials of the same decay parameter and well depth, showing that these are typically 10% too large, although having the right trends. Last, we note the serious overestimate in the semiclassical results for the light particles, as expected, and we discuss the origin of this effect later. Note that if the semiclassical analysis were to be accurate even for those masses, it would yield a ratio of β 's for D_2 to H_2 of $\sqrt{2}$, or 1.41, whereas the experimental result is 1.76.

Next we plot $\beta\sqrt{m_{\text{Ar}}/m}$ as a function of $E_{\text{eff}}^{3/2}$ for the two cases for which we varied the incident energy, Ne and Ar, in Fig. 10. Here the theory agrees exceedingly well over the entire range, reproducing the energy dependence for both atoms. Again, the Morse potential typically leads to a 10% overestimate. The worst case is $E_{\perp}=30$ meV for Ne, which we show below has a larger error due to density-of-states effects. Note the approximate linearity within each set of data (Ne and Ar), demonstrating the qualitatively correct nature of the effective exponential model.

Similarly, in Fig. 11 we plot $2W(0)$ versus m , which an effective exponential repulsion gives as being proportional to E_{eff}^2 and independent of the mass. We scale $2W(0)$ by

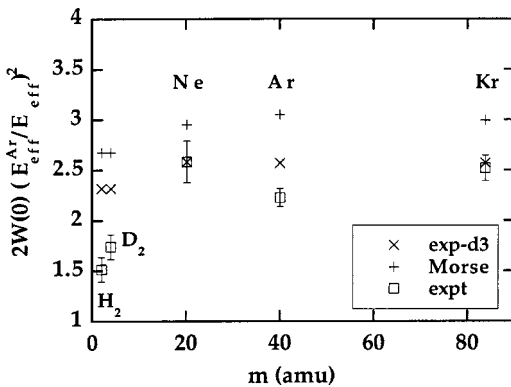


FIG. 11. Zero-temperature Debye-Waller factor, $2W(0)$, as a function of m , scaled by E_{eff}^2 . The points at $m=4$ refer to D_2 .

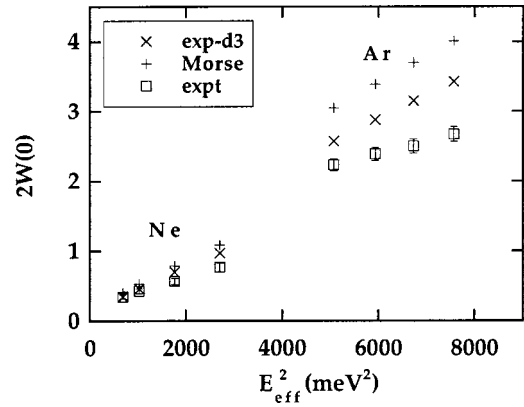


FIG. 12. Zero-temperature Debye-Waller factor, $2W(0)$, as a function of E_{eff}^2 , for incident Ne and Ar atoms.

$(E_{\text{eff}}^{\text{Ar}}/E_{\text{eff}})^2$, where $E_{\text{eff}}^{\text{Ar}}=71.2$ meV. Again, the agreement fails for lighter particles, the mass independence is reproduced, and the Morse potential yields a consistent overestimate of the results. If the semiclassical limit applied, $2W(0)$ would be the same for both H_2 and D_2 , whereas it changes by more than 10%.

Next we plot $2W(0)$ versus E_{eff}^2 for Ne and Ar in Fig. 12. We first note that the overall trends agree with the experiment, but that the quantitative error is much greater than for β . This error grows as E_{eff} increases. In the section below, we show that this is due to density-of-states effects, which are more prominent in $2W(0)$ than in β . Note, also in this case, the approximate linearity within each set of data (Ne and Ar), demonstrating the qualitatively correct nature of the effective exponential model.

C. Deviations from semiclassical limit

In this section, we consider the various sources of error in our calculations, and estimate them. We find that we are either in the large-mass limit, or close to it, in these experiments.

1. Driven oscillator model

The most egregious failure of theory here would be if the driven oscillator model [Eq. (1)] did not apply. The driven oscillator model treats the incident particle as providing a time-dependent driving force on the phonons at the surface. Even at zero surface temperature, some phonons gain energy, and the elastic fraction is reduced. In the exponentiated distorted-wave Born approximation, this driving force is (inconsistently) approximated by that due to a recoilless collision, but still yields the correct loss spectrum for weakly inelastic scattering, as demonstrated in Ref. 9. If the scattering is too strong, i.e., if the fractional energy loss of the incident particle is too big, these matrix elements will not be accurately approximated by their recoilless counterparts, and there is no general solution to the quantum scattering problem. We use Eq. (10) to calculate the mean energy loss, ΔE , which we tabulate in Table III. In most cases, the mean energy loss is a small fraction of the effective incident energy. The worst offender is Kr, which loses about 40% of its ef-

TABLE III. Results for $2W(0)$, β , and $\hbar\bar{\omega}=2k_B 2W(0)/\beta$, both experimental and semiclassical theory calculations, with the effective spectral function discussed in Sec. V C 2. ΔE is the calculated mean energy loss.

		$2W(0)$		β (K^{-1})		ΔE (meV)		$\hbar\bar{\omega}$ (meV)	
		Calc.	Expt.	Calc.	Expt.	Calc.	Calc.	Expt.	Expt.
m (amu)		$E_{\perp}=4.2$ meV							
H ₂	2.0	0.12	0.34	0.0021	0.0033	1.5	9.8	17.8	
D ₂	4.0	0.23	0.39	0.0043	0.0058	2.5	9.2	11.6	
He	4.0	0.03	0.10	0.0009	0.0014	0.3	5.7	12.3	
Ne	20.2	0.33	0.35	0.0105	0.0109	2.3	5.4	5.5	
Ar	40.0	2.30	2.23	0.0652	0.0670	18.2	6.1	5.7	
Kr	83.8	5.25	5.40	0.1716	0.1670	36.5	5.3	5.6	
E_{\perp} (meV)									
Ne	4.2	0.33	0.35	0.0105	0.0109	2.3	5.4	5.5	
Ne	10.0	0.43	0.43	0.0132	0.0133	3.2	5.6	5.6	
Ne	20.0	0.62	0.57	0.0182	0.0183	4.9	5.9	5.4	
Ne	30.0	0.82	0.77	0.0235	0.0230	6.8	6.0	5.8	
Ar	4.2	2.30	2.23	0.0652	0.0670	18.2	6.1	5.7	
Ar	10.0	2.54	2.39	0.0710	0.0728	20.4	6.2	5.7	
Ar	15.0	2.75	2.50	0.0761	0.0788	22.3	6.2	5.5	
Ar	20.0	2.96	2.67	0.0813	0.0841	24.3	6.3	5.5	

fective perpendicular energy. This will lead to small modifications in its trajectory during most of the collision, but of course suggests a large prompt sticking coefficient, since after the collision, it will (on average) have too little energy to escape the physisorption well.

2. Density of states and cutoff effects

The most significant error we could find in our calculations is due to the long-wavelength limit assumption for the density of states of the surface response. From Fig. 1, it is clear that the driving force has a long tail, well beyond its peak, stretching into regions of phonon frequency well beyond the low-frequency limit.

Deviations from our model then occur for two distinct reasons: First, the phonon spectral response function deviates from a linear behavior and eventually drops to zero; second, there can be significant parallel momentum transfer, which is modeled, however, by a cutoff factor of form $\exp(-Q^2/Q_c^2)$ (see Sec. II B) in an effective spectral function. In Fig. 13, we plot the spectral function, the effective spectral function, and the extrapolation assumed by using the continuum limit. The slope (value of C_s) is taken from Ref. 4, as the phonon model there¹⁸ was designed to be accurate for shorter wave vectors rather than long ones. We see that the continuum model remains an accurate approximation up to about 13 meV, after which the effective spectral function drops dramatically. It is interesting that the parallel momentum transfer damping effects in fact make the low-frequency limit valid up to much higher frequencies than for the undamped spectral function. Note that the cutoff factor was calculated for H₂ (D₂) scattering¹⁸ and depends on both the classical turning point and decay of the repulsion, so that it can only be regarded as an estimate for our conditions.

We have rerun our calculation with the effective spectral function inserted in Eq. (1), with results given in Table III. The DOS effects reduce the integrals and improve the agreement with experiment. In particular $2W(0)$, which is more sensitive to the high-energy part of the phonon spectrum, is significantly improved for all heavy-atom collisions and is now accurate to within 10% for the E_{\perp} range studied, while β is good to within 3%. This is in remarkably good agreement for a comparison with no adjustable parameters.

3. Classical limit of matrix elements

Given that the driven oscillator model applies, we next check that the semiclassical limit has been reached for the matrix elements in Eq. (1), i.e., to see if the wavelength of the incident particles is sufficiently short. Since we need only

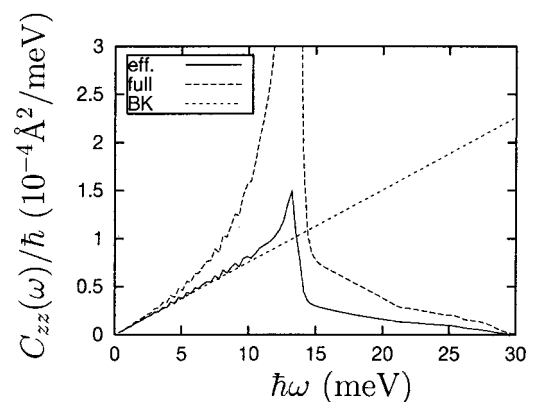


FIG. 13. Cu(111) surface spectral function: effective function involving cutoff factor, full function, and extrapolated function from continuum limit.

an estimate, we use the effective exponential repulsion model, for which the quantum-mechanical matrix elements are known, e.g., Eq. (46) of Ref. 9:

$$F_{\perp}(\omega) = p_{\perp} 2\pi\omega\tau \sqrt{\sinh^{-2}(\pi\Delta kd) - \sinh^{-2}[\pi(2k - \Delta k)d]}, \quad (19)$$

where Δk is the perpendicular wave vector loss and k is the initial perpendicular value. Noting that, for small energy transfer, $\Delta kd \approx \hbar\omega\tau$, we can write

$$F_{\perp}(\omega) = F_{\perp}^{\text{class}}(\omega) \sqrt{1 - \left(\frac{\sinh(\pi\hbar\omega\tau)}{\sinh[\pi(4E - \hbar\omega)\tau]} \right)^2}. \quad (20)$$

We may use $\hbar\bar{\omega}$ as a measure of the typical phonon excitation energy in the collision, and take τ_{eff} and E_{eff} from the effective exponential repulsion. We find in almost every case that the acceleration due to the attractive well makes the term $4E_{\text{eff}} - \hbar\bar{\omega}$ so much greater than $\hbar\bar{\omega}$ that the correction is exponentially small. The sole exception is the He-atom case, where $\hbar\bar{\omega}$ is about 12 meV, while E_{eff} is about 10 meV. Such conditions are typical of the more standard highly quantum-mechanical scattering experiments. Interestingly, because of the large well depth, the matrix elements for both H_2 and D_2 scattering are very well approximated by their classical values.

VI. CONCLUSIONS

The elastic scattering of slow heavy atoms from solid surfaces exhibits some strikingly simple behavior according to a semiclassical description of the Debye-Waller factor. The model predicts that the Debye-Waller exponent is independent of particle mass m at low surface temperatures and depends on \sqrt{m} at elevated temperatures. We find from our experiments involving low-energy nozzle beams of Ne, Ar, and Kr scattering from a Cu(111) surface that the measured elastic scattering behavior is consistent with the predicted mass dependencies. Calculations of the Debye-Waller exponent, using appropriate physisorption potentials, yield quantitative agreement with the experimental data both at low and high surface temperature. We also find these predictions to be violated for the lighter particles scattering from the same surface.

Most experiments and calculations of atoms striking solid surfaces are performed with light fast particles (thermal energy He beams) in which the wavelength of the incident particle is comparable to the dimensions of the surface. In

such a regime, the incident particle behaves as a wave, and simple kinematics yields much useful information: positions of diffraction peaks yield surface geometries, positions of bound-state resonances yield potential-shape information, and positions of one-phonon peaks yield dispersion relations for phonons at the surface. The regime studied in this paper complements this very well. For heavy, slow atom scattering, another simple, but complementary, picture emerges. Classical mechanics is sufficient to determine the dynamics, while an elastic continuum model of the crystal suffices to determine its response. Instead of information about short-wavelength single phonons, we garner long-wavelength information about all phonons; instead of information about individual bound states, we find integrals over the entire potential. The combination of this information with bound-state information provides a vital independent test of models for physisorption potentials and models of phonons at surfaces.

Our results also provide a dramatic verification of the usefulness of the driven oscillator model (also known as the exponentiated Born approximation) for atom-surface interactions. None of these results can be explained by one-phonon-type scattering descriptions, even qualitatively. Under the right conditions (i.e., small relative energy loss of the incident particle), this model accurately predicts the strongly inelastic scattering of atoms from surfaces. Thus, we have shown that multiphonon effects can be accurately predicted from theory and understood in experiments.

Last, we point out that, at the lowest E_{\perp} , the ratio $2W(0)/\beta$ is given to within 13% by our classical calculations, ignoring any density-of-states effects. This ratio is completely independent of *any* surface details, according to the theory, and depends only on the classical trajectory of the incoming particle in the physisorption well. Thus we have a new, very robust test of any models of such wells. Remarkably, we also find that continuum limit calculations of β are accurate to within 3% and apparently provide another sensitive test of potential models.

ACKNOWLEDGMENTS

We thank B. Gumhalter, A. Luntz, M. Persson, and B. Jackson for useful discussions and comments about this work. Financial support from the Swedish Natural Science Research Council and the Swedish Research Council for Engineering Sciences is gratefully acknowledged. K.B. was partially supported by the National Science Foundation under Grant No. CHE-9875091.

¹G. Benedek and J. P. Toennies, *Surf. Sci.* **299/300**, 587 (1994).

²See, e.g., the discussions in Refs. 3 and 4 and references therein.

³A. C. Levi and H. Suhl, *Surf. Sci.* **88**, 221 (1979).

⁴K. Burke and W. Kohn, *Phys. Rev. B* **43**, 2477 (1991).

⁵F. Althoff, T. Andersson, and S. Andersson, *Phys. Rev. Lett.* **79**, 4429 (1997).

⁶A. Siber and B. Gumhalter, *Phys. Rev. Lett.* **81**, 1742 (1998).

⁷F. Althoff, T. Andersson, and S. Andersson, *Phys. Rev. Lett.* **81**, 1743 (1998).

⁸T. Andersson, F. Althoff, P. Linde, M. Hassel, M. Persson, and S. Andersson, *J. Chem. Phys.* **113**, 9262 (2000).

⁹K. Burke, B. Gumhalter, and D. C. Langreth, *Phys. Rev. B* **47**, 12 852 (1993).

¹⁰G. Armand and J. R. Manson, *Surf. Sci.* **80**, 532 (1979).

- ¹¹A. Chizmeshya and E. Zaremba, *Surf. Sci.* **268**, 432 (1992).
- ¹²The position of the He-Cu potential predicted by Chizmeshya and Zaremba is debated; see J. Ellis, K. Hermann, F. Hofmann, and J. P. Toennies, *Phys. Rev. Lett.* **75**, 886 (1995). Our results though, do not depend on the choice of origin.
- ¹³S. Andersson and M. Persson, *Phys. Rev. B* **48**, 5685 (1993).
- ¹⁴J. Perreau and J. Lapujoulade, *Surf. Sci.* **122**, 341 (1982).
- ¹⁵T. Andersson, P. Linde, and S. Andersson (unpublished).
- ¹⁶J. Unguris, L. W. Bruch, and M. B. Webb, *Surf. Sci.* **114**, 219 (1982).
- ¹⁷C.-F. Yu, K. B. Whaley, C. S. Hogg, and S. J. Sibener, *Phys. Rev. Lett.* **51**, 2210 (1983).
- ¹⁸S. Andersson and M. Persson, *Phys. Rev. Lett.* **70**, 202 (1993). More sophisticated interatomic force models for copper are discussed in G. Santoro, A. Franchini, V. Bortolani, D. L. Mills, and R. F. Wallis, *Surf. Sci.* **478**, 99 (2001).
- ¹⁹H.-J. Ernst, F. Charra, and L. Douillard, *Science* **279**, 679 (1998).
- ²⁰S. Andersson, L. Wilzen, M. Persson, and J. Harris, *Phys. Rev. B* **40**, 8146 (1989).
- ²¹See e.g., B. Poelsema and G. Comsa, *Scattering of Thermal Energy Atoms from Disordered Surfaces*, Springer Tracts in Modern Physics No. 115 (Springer, Berlin, 1989).
- ²²J. F. Ready, *Effects of High Power Laser Radiation* (Academic, New York, 1971).
- ²³J. H. Bechtel, *J. Appl. Phys.* **46**, 1585 (1975).
- ²⁴Weak diffraction peaks may persist for more corrugated surfaces as reported for Ar scattering from 2H-W(100) at 90 K by E. K. Schweizer and C. T. Rettner, *Phys. Rev. Lett.* **62**, 3085 (1989).
- ²⁵G. Boato, P. Cantini, and L. Mattera, *J. Chem. Phys.* **65**, 544 (1976).
- ²⁶Determination of β and extrapolation of $\ln I_{00}$ to $T=0$ K involves only those data points that give an optimum fit to a linear decay of $\ln I_{00}$ with T which means data at $T \geq 300, 130, 80,$ and 50 K for He, Ne, Ar, and Kr, respectively, and $T \geq 250$ and 175 K for H_2 and D_2 .